Journal of Materials Research and Technology 42 (2026) 2625–2637

Contents lists available at ScienceDirect

Journal of Materials Research and Technology

journal homepage: www.elsevier.com/locate/jmrt

Formation of a bi-directional α_2/γ lamellar microstructure through crystallographic texture control in a γ-TiAl alloy fabricated by laser powder bed fusion

Sung-Hyun Park [a], Ozkan Gokcekaya [b,c], Kazuhisa Sato [d], Ji-Sung Park [a], Chae-Won Kim [a], Myung-Hoon Oh [e], Seong-Woong Kim [a,*], Takayoshi Nakano [b,c,**]

[a] Extreme Materials Research Institute, Korea Institute of Materials Science (KIMS), Changwon, 51508, Republic of Korea
[b] Division of Materials and Manufacturing Science, Graduate School of Engineering, The University of Osaka, 2-1, Yamadaoka, Suita, Osaka, 565-0871, Japan
[c] Anisotropic Design & Additive Manufacturing Research Center, The University of Osaka, 2-1, Yamadaoka, Suita, Osaka, 565-0871, Japan
[d] Research Center for Ultra-High Voltage Electron Microscopy, The University of Osaka, 7-1 Mihogaoka, Ibaraki, Osaka, 567-0047, Japan
[e] School of Materials Science and Engineering, Kumoh National Institute of Technology (KIT), 61 Daehakro, Gumi, Gyeongbuk, 39177, Republic of Korea

ARTICLE INFO

Keywords:
γ-titanium aluminide
Laser powder bed fusion
Crystallographic texture
Peritectic reaction
Directional lamellar microstructure

ABSTRACT

This study presents, for the first time, a bi-directional α_2/γ lamellar microstructure achieved in a γ-titanium aluminide (γ-TiAl) alloy via laser powder bed fusion (LPBF). In the as-built condition, the microstructure was predominantly composed of the α_2 phase, in which a crystallographic lamellar microstructure (CLM) consisting of two differently oriented crystallographically textured layers was established. In the major layer, the {0001} direction was oriented perpendicular to the building direction (BD), whereas in the minor layer, it was nearly aligned parallel to the BD. After heat treatment the previously formed CLM was preserved, thereby governing the orientation of the subsequently formed α_2/γ lamellae according to the Blackburn orientation relationship. Therefore, a bi-directional α_2/γ lamellar microstructure was obtained, with lamellae oriented parallel (0°) and perpendicular (90°) to the BD in the major and minor layers, respectively. The individual nano-hardness measurements revealed values of 9.3 ± 0.4 GPa for the major layer and 10.4 ± 0.8 GPa for the minor layer, which are much higher than those of γ-TiAl alloys produced by other processing methods. This unique microstructural formation was primarily enabled by a peritectic reaction-based alloy design combined with process-induced crystallographic texture control, highlighting a new pathway for microstructural design of γ-TiAl alloys and potentially enabling improved mechanical performance.

1. Introduction

γ-titanium aluminide (γ-TiAl) alloys are considered promising lightweight structural materials for high-temperature applications due to their excellent creep resistance and oxidation stability [1,2]. Notably, γ-TiAl alloys have successfully replaced Ni-based superalloys in the intermediate temperature environments (~750 °C) [2,3]. However, despite these advantages, the operational temperature limit of γ-TiAl alloys has remained stagnant for several decades, and extending their temperature capabilities is still a significant challenge [2].

One effective approach to achieving a breakthrough in the high-temperature mechanical performance of γ-TiAl alloys is to obtain lamellar structures with a parallel orientation (0°) to the loading direction through directional solidification (DS) techniques [4]. The use of a specific seed alloy in the DS technique is one of the fundamental approaches for controlling lamellar orientation [5,6]. However, the seed materials must meet critical requirements [6–8], and the compositional differences between master alloys and seed materials lead to issues such as uneven compositional distribution, which can lead to compositional inhomogeneity and potentially deteriorate the properties of the produced materials. Moreover, DS techniques require strict control of processing conditions, and it is difficult to fabricate large components with complex shapes.

Meanwhile, additive manufacturing (AM) enables the direct

* Corresponding author. Extreme Materials Research Institute, Korea Institute of Materials Science (KIMS), Changwon 51508, Republic of Korea.
** Corresponding author. Division of Materials and Manufacturing Science, Graduate School of Engineering, The University of Osaka, 2-1, Yamadaoka, Suita, Osaka, 565-0871, Japan.
E-mail addresses: mrbass@kims.re.kr (S.-W. Kim), nakano@mat.eng.osaka-u.ac.jp (T. Nakano).

https://doi.org/10.1016/j.jmrt.2026.03.273
Received 3 February 2026; Received in revised form 12 March 2026; Accepted 30 March 2026
Available online 31 March 2026

fabrication of near-net-shaped components from three-dimensional computer-aided design data through layer-by-layer powder fusion using a scanning heat source [9], and has recently emerged as an advanced manufacturing technique for a wide range of metallic materials, such as titanium, aluminium, nickel, and magnesium alloys [10–13]. In laser powder bed fusion (LPBF), a representative AM technique, products are manufactured by stacking the melt pools generated by focused beams as individual units. Steep thermal gradients are inherently formed within these melt pools, allowing crystallographic texture control through adjustment of the melt pool geometry [14,15]. The formation and control of the crystallographic texture using the LPBF have been demonstrated to be highly effective in tailoring the performance of various metallic materials [16–21]. Therefore, LPBF can be considered a promising platform for achieving single-crystal-like microstructural control beyond conventional DS techniques, offering new opportunities for controlling lamellar orientation in γ-TiAl alloys.

However, studies on lamellar orientation control in γ-TiAl alloys processed by LPBF remain limited, as the intrinsic brittleness of these alloys has directed most research efforts toward understanding cracking mechanisms and achieving high densification during processing [22–25]. Furthermore, the microstructures reported to date are predominantly polycrystalline with random orientations [26,27], and such microstructures are not fundamentally different from those obtained by conventional processing routes, including casting followed by cyclic heat treatments or hot working with subsequent microstructural control [28–30]. In addition, the repetitive thermal cycles and rapid cooling rates associated with AM further complicate lamellar orientation control in γ-TiAl alloys undergoing complex phase transformations.

Nevertheless, a limited number of recent studies have demonstrated both the feasibility and effectiveness of fabricating directionally aligned lamellar microstructure in γ-TiAl alloys by AM, particularly using the direct laser deposition (DLD) process [31,32], while, to the best of our knowledge, lamellar orientation control in γ-TiAl alloys processed by LPBF has not yet been reported. The motivation for employing LPBF lies in its ability to locally tailor lamellar orientation via spatially controlled melt pool interactions, enabling location-specific microstructural control, thereby offering greater design freedom than DLD.

Here, we demonstrate a bi-directional α_2/γ lamellar microstructure in a γ-TiAl alloy processed by LPBF, achieved through a peritectic reaction–based alloy design combined with process-induced crystallographic texture. This work elucidates the mechanisms of lamellar orientation control in LPBF-processed γ-TiAl alloys and provides insights relevant to enhanced mechanical performance.

2. Materials and methods

2.1. Raw powder characteristics and sample fabrication

Fig. 1(a and b) shows the particle size distribution and a representative image of the spherical γ-TiAl alloy powder prepared by gas atomization. The powder had a median particle size (d_m) of 30.4 μm and a nominal composition of Ti-46Al-6Nb-0.5W-0.5Cr-0.3Si-0.1C (at.%, KIMS #16 alloy). As shown in Fig. 1(c), cubic samples with dimensions of 5 mm (depth) x 5 mm (length) x 5 mm (height) were fabricated using an LPBF machine (EOS M290, EOS, Germany). The bidirectional scanning strategy along the x-axis was applied with laser power, scanning speed, hatch distance, and layer thickness of 180 W, 1000–1800 mm/s, 80–100 μm, and 40–60 μm, respectively. The building chamber was filled with argon gas to avoid a reaction, and the baseplate was preheated to 200 °C.

2.2. Characterization

The as-built specimens were sectioned, and the cross sections were mechanically polished using emery papers, followed by final polishing with colloidal silica. The relative density of the fabricated specimens was evaluated using an optical microscope (OM; BX60, Olympus, Japan) and ImageJ software. The microstructures of specimens were observed by a field-emission scanning electron microscope (FE-SEM; JIB-4610F, JEOL, Japan) equipped with an electron backscatter diffraction system (EBSD; NordlysMax^3, Oxford Instruments, UK). To investigate the microstructural evolution after heat treatment, heat treatment was conducted at 800 °C for 3 h followed by air cooling. Prior to heat treatment, the specimens were sealed in a quartz tube. After heat treatment, microstructural characterization was performed using the same procedures as those applied to the as-built specimens. In addition, the phase constitution of the samples was analyzed by X-ray diffractometry (XRD; X'pert PRO, Philips, The Netherlands) using a Cu target at an acceleration voltage of 40 kV and a current of 30 mA, and further analysis was conducted using a transmission electron microscope (TEM; JEM-ARM200F, JEOL, Japan). Mechanical properties were evaluated by nanoindentation tests (ENT-1100a, ELIONIX, Japan) with a maximum load of 4.9 mN and a holding time of 10 s, employing a Berkovich indenter.

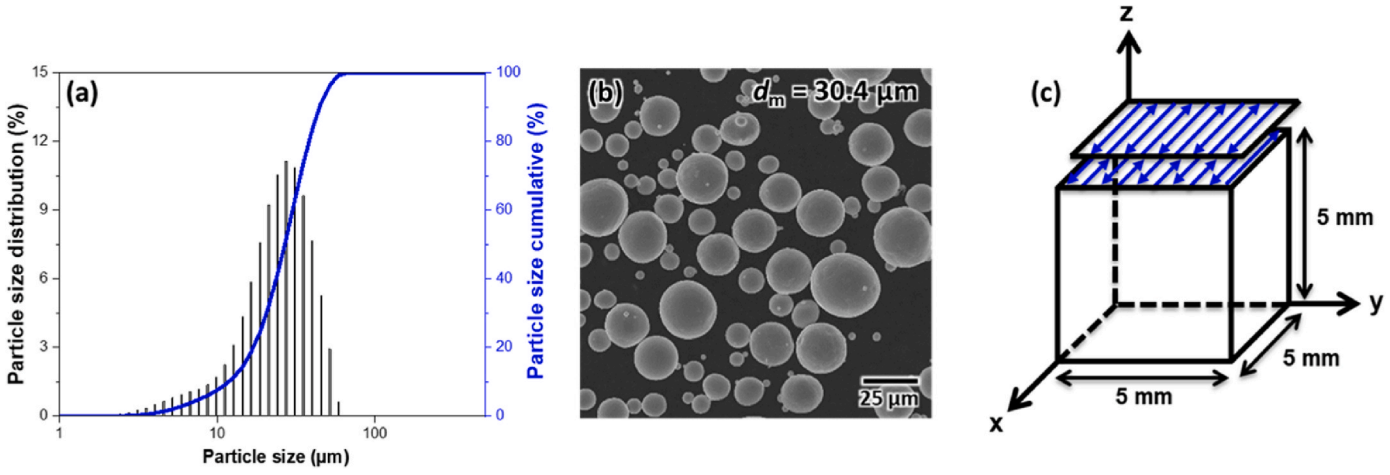

Fig. 1. (a) Particle size distribution of the raw powder, (b) typical SEM image of the γ-TiAl alloy powder used in this study, and (c) schematic illustration of the specimen dimensions and the applied scanning strategy.

3. Results and discussion

3.1. Phase transformation in γ-TiAl alloys and alloy design for crystallographic texture control by LPBF

In the γ-TiAl alloy, the solidification modes are generally classified as β, peritectic, and α solidification depending on the alloy composition [33,34]. As summarized in Table 1, although the primary solidification phase and the subsequent transformation sequence differ, the β → α and α → γ phase transformations during solidification follow well-defined phase relationships between the constituent phases. That is, the β → α transformation follows the Burgers orientation relationship (Burgers OR) where $\{110\}_\beta//(0001)_\alpha$ and $<111>_\beta//<11\,\bar{2}\,0>_\alpha$, while the α → γ transformation follows the Blackburn orientation relationship (Blackburn OR) where $\{0001\}_{\alpha2}//\{111\}_\gamma$ and $<11\ \bar{2}\ 0>_{\alpha2}//<1\ \bar{1}\ 0>_\gamma$, respectively [35,36]. Therefore, the final α_2/γ lamellar orientation is determined by the crystallographic texture of the primary phase and the orientation relationships between the constituent phases during subsequent phase transformations.

While β-solidified γ-TiAl alloys theoretically involve up to twelve possible α variants during the β → α phase transformation, these α variants do not transform with equal probability, a phenomenon commonly referred to as variant selection. This variant selection is influenced by various factors, including transformation-induced shape strain and interfacial energy [37,38], which makes the formation of a single α variant difficult to achieve. In addition, processing-related factors, particularly the high cooling rates characteristic of AM, promote massive transformation, which in turn leads to the development of weak and randomly oriented crystallographic textures [23,39]. As a result, the lamellar orientation in β-solidified γ-TiAl alloys cannot be effectively controlled owing to the complex β → α transformation behavior.

In contrast, α-solidified γ-TiAl alloys undergo a relatively simple phase transformation during solidification and exhibit preferential growth of the α phase along the <0001> direction due to its hexagonal crystal structure [6,40], which is expected to facilitate lamellar orientation control. However, variations in scanning strategy and the associated changes in melt pool geometry in LPBF do not significantly affect the resulting crystallographic texture formation. The {0001} orientation remains predominantly aligned parallel to the building direction (BD), independent of the scanning strategy [41]. This behavior originates from the crystal symmetry of the hexagonal phase, specifically the limited multiplicity of preferential growth directions of the cells, which governs crystallographic texture development in the LPBF.

Therefore, a peritectic-solidified γ-TiAl alloy, the KIMS #16 alloy, was designed in the present study. As illustrated in Fig. 2(a), the most significant difference from other solidification modes is the presence of a three-phase region (L + β + α), which is enabled by the addition of β-stabilizing elements [6,42]. In addition, the peritectic α phase nucleates at the interface between the primary β phase and the liquid (Fig. 2 (b)), and its orientation is inherited from the primary β phase through the Burgers OR [43]. According to the orientation relationships between the β and α phases described above, twelve possible α variants with different growth directions can theoretically form during the solid-state phase transformation. However, only one of these variants is preferentially selected to envelop a given β phase through the peritectic reaction, leading to the formation of coarse columnar grains. We therefore hypothesize that this solidification pathway promotes the development of a strong crystallographic texture during the LPBF, while offering greater flexibility for crystallographic texture control through variations in melt pool geometry.

Table 1
Solidification modes and corresponding phase transformation sequences in γ-TiAl alloys.

Solidification mode	Phase transformation sequence
β solidification	L → L+ β → β → β + α → α → α + γ
Peritectic solidification	L → L+ β → L+ β + α → (β + α, L + α) → α → α + γ
α solidification	L → L+ α → α → β + α → α → α + γ

3.2. Effect of LPBF process parameters on densification and microstructural characteristics

In order to explore the effect of LPBF process parameters on densification, specimens were fabricated under various processing conditions. Fig. 3(a) presents the relative density of the fabricated samples as a function of the applied volumetric energy density (VED), which is defined as

$$\mathrm{VED} = \frac{P}{\nu d t} \tag{1}$$

Where P is the laser power, ν is the scanning speed, d is the hatch distance, and t is the layer thickness. A general increase in relative density was observed with increasing VED. Nevertheless, fully crack-free specimens were not achieved within the investigated processing window, which is attributed to the high crack susceptibility of intrinsically brittle γ-TiAl alloys. The highest relative density of 97.0 ± 0.4% was obtained at a VED of 38 J/mm^3 (t: 0.06). As shown in Fig. 3(b and c), the OM images indicate that cracks distributed in the cross-section of the y–z plane were the main defects limiting high densification. In addition, most cracks were oriented parallel to the BD, while curved crack morphologies were also observed.

Fig. 4 presents SEM–EBSD results obtained from the crack region to further understand the origin of these cracks. As indicated by the arrows in the band contrast image, distinct cracks can be clearly observed in the analyzed region (Fig. 4(a)). The corresponding phase map reveals the presence of the γ phase formed around the crack region, highlighted by the blue circle (Fig. 4(b)). Furthermore, the inverse pole figure (IPF) map shown in Fig. 4(c) indicates that the cracks are preferentially located along the boundaries between differently oriented columnar grains. These columnar grain boundaries exhibit a high misorientation angle of 89° and 81° (Fig. 4(d)), suggesting that the key factors of crack initiation in the present study are associated with the presence of the γ phase and high-angle grain boundaries (HAGBs).

During the LPBF process, the fabricated specimens experience repeated melting and solidification under complex thermal histories. In particular, the previously solidified regions can be affected by heat accumulation from adjacent or upper scan tracks. As a result, several phases coexist in γ-TiAl alloys fabricated by the LPBF process, and high thermal residual stresses occurring at the interfaces between these different phases can act as driving factors for crack formation [22,27]. This is mainly attributed to the mismatch in the coefficients of thermal expansion (CTE) among the β,α_2, and γ phases in γ-TiAl alloys. The differences in CTE become larger during the cooling [44], which can generate significant local stresses at the phase interfaces, making these regions potential sites for crack initiation. Moreover, previous studies reported that HAGBs are favorable locations for crack nucleation due to stress concentration [17,19], as the large misorientation between adjacent grains impedes slip transfer and causes localized stress accumulation at the grain boundaries. Therefore, optimizing the process parameters to minimize phase transformations and promote the formation of a single-phase microstructure with strong crystallographic texture is beneficial, as it reduces the fraction of HAGBs, which may facilitate densification.

Fig. 5 shows phase maps, IPF maps colored according to the crystallographic orientation along the y-direction, and the corresponding {0001} pole figures (PFs) of the α_2 phase for several process parameter conditions. In the phase map (Fig. 5(a–d)), the volume fraction of the γ phase formed due to the heat accumulation effect from adjacent scan tracks decreased from 19.6% to 1.5% with increasing ν and decreasing t, resulting in a microstructure closer to a single-phase condition.

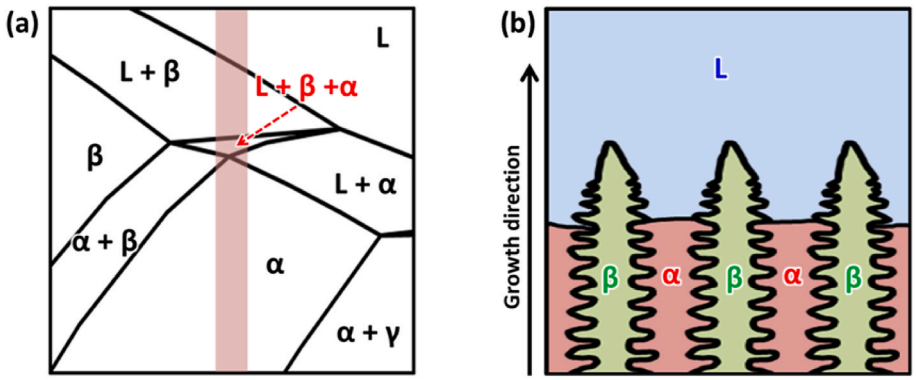

Fig. 2. (a) Schematic phase diagram of the ternary Ti–Al–M system, where M denotes a β-stabilizing element, and (b) schematic illustration of the growth morphologies of the α and β phases during the peritectic reaction.

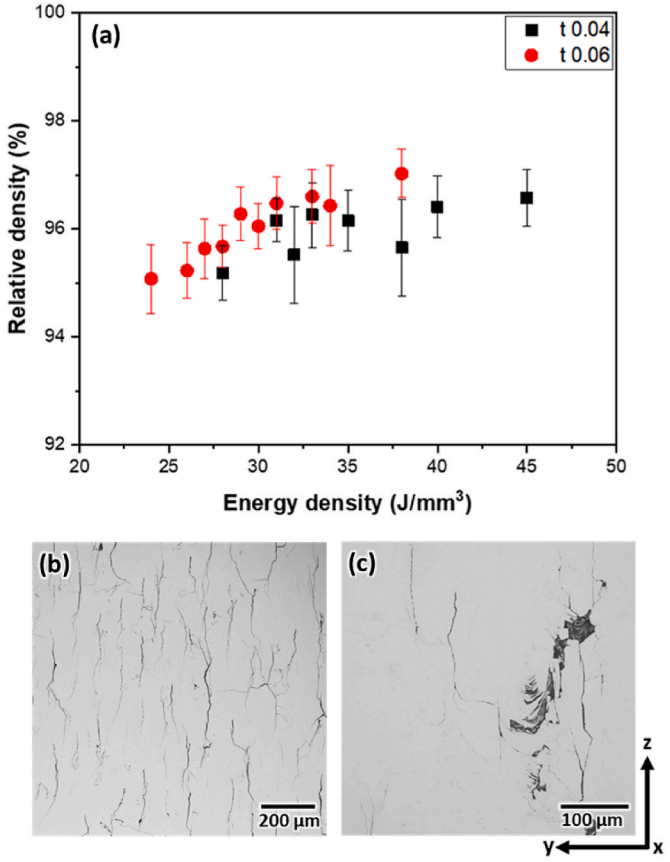

Fig. 3. (a) Relationship between the relative density and VED. (b, c) OM images of the y–z cross-sections of the samples showing representative cracking behavior.

Moreover, as confirmed from the IPF maps and PFs (Fig. 5(e–l)), the {0001} direction was alternately oriented either perpendicular or parallel to the BD, indicating the formation of a crystallographic lamellar microstructure (CLM). Such layered structures in three-dimensional space are closely associated with the melt pool geometry during the LPBF process [45,46], and the detailed formation mechanisms will be discussed in a later section.

Meanwhile, at a relatively low *v* of 1200 mm/s (Fig. 5(e)), an inhomogeneous CLM was observed in the IPF maps, although the PF indicated the presence of two dominant orientations (Fig. 5(i)). Furthermore, the fine equiaxed γ phase formed within the α_2 phase regions, which weakened the crystallographic texture. On the other hand, when the *v* increased to 1400 mm/s, the volume fraction of the γ phase decreased, leading to a reduction in crystallographic texture weakening. Moreover, the {0001} orientation perpendicular to the BD became more dominant than the parallel orientation (Fig. 5(j)). However, the increase in *v* also caused a reduction in the melt pool depth (D), resulting in locally unstable crystallographic texture formation and epitaxial growth along the BD, as indicated by the black arrows (Fig. 5(f)). To improve this instability, the *t* was reduced to 0.04 mm, which promoted stable epitaxial growth and a more uniform crystallographic texture along the BD (Fig. 5(g, k). Lastly, when the *v* was further increased to 1600 mm/s, the additional decrease in D again resulted in unstable crystallographic texture formation (Fig. 5(h, l).

Additional observations of the melt pool geometry as a function of *v* further support the previously observed microstructural characteristics (Fig. 6). At a relatively low v of 1200 mm/s, a wider melt pool width (W) was formed. Under a *d* of 0.08 mm, the overlapping melt pool region became relatively large, which promoted the formation of equiaxed γ phases and resulted in an inhomogeneous crystallographic texture due to excessive heat accumulation and remelting. In contrast, at a *v* of 1400 mm/s, an optimal remelting condition together with a sufficient D under a reduced *t* of 0.04 mm led to the formation of a stable crystallographic texture with a minimal fraction of the γ phase. However, when the *v* was further increased to 1600 mm/s, insufficient remelting occurred due to the reduced W and D, resulting in unstable crystallographic texture formation despite the reduced γ phase fraction. Consequently, the optimal condition in this study was determined to be a *P* of 180 W, a *v* of 1400 mm/s, a *d* of 80 μm, and a *t* of 40 μm. Although this condition did not exhibit the highest relative density, it still showed a relatively high densification of 96.4 ± 0.6%. More importantly, it provided the most stable crystallographic texture with a low fraction of the γ phase.

It should be noted that further improvement in relative density is still required for practical applications. However, the primary focus of the present study is on crystallographic texture and lamellar orientation control rather than on densification optimization. To achieve high densification in LPBF-processed γ-TiAl alloys, several studies have employed strategies such as the addition of nanoparticles or circular oscillating scanning to promote the formation of fine equiaxed grains [26,47]. Such equiaxed microstructure can more effectively accommodate strain and suppress the crack formation compared to columnar microstructures [48]. However, nanoparticles-induced equiaxed grain formation is accompanied by increased randomness in crystallographic texture [25,47], which hinders the formation of an aligned lamellar microstructure. Alternatively, the application of a high substrate preheating temperature may be considered as a feasible approach to further improve the relative density of LPBF-processed γ-TiAl alloys [49].

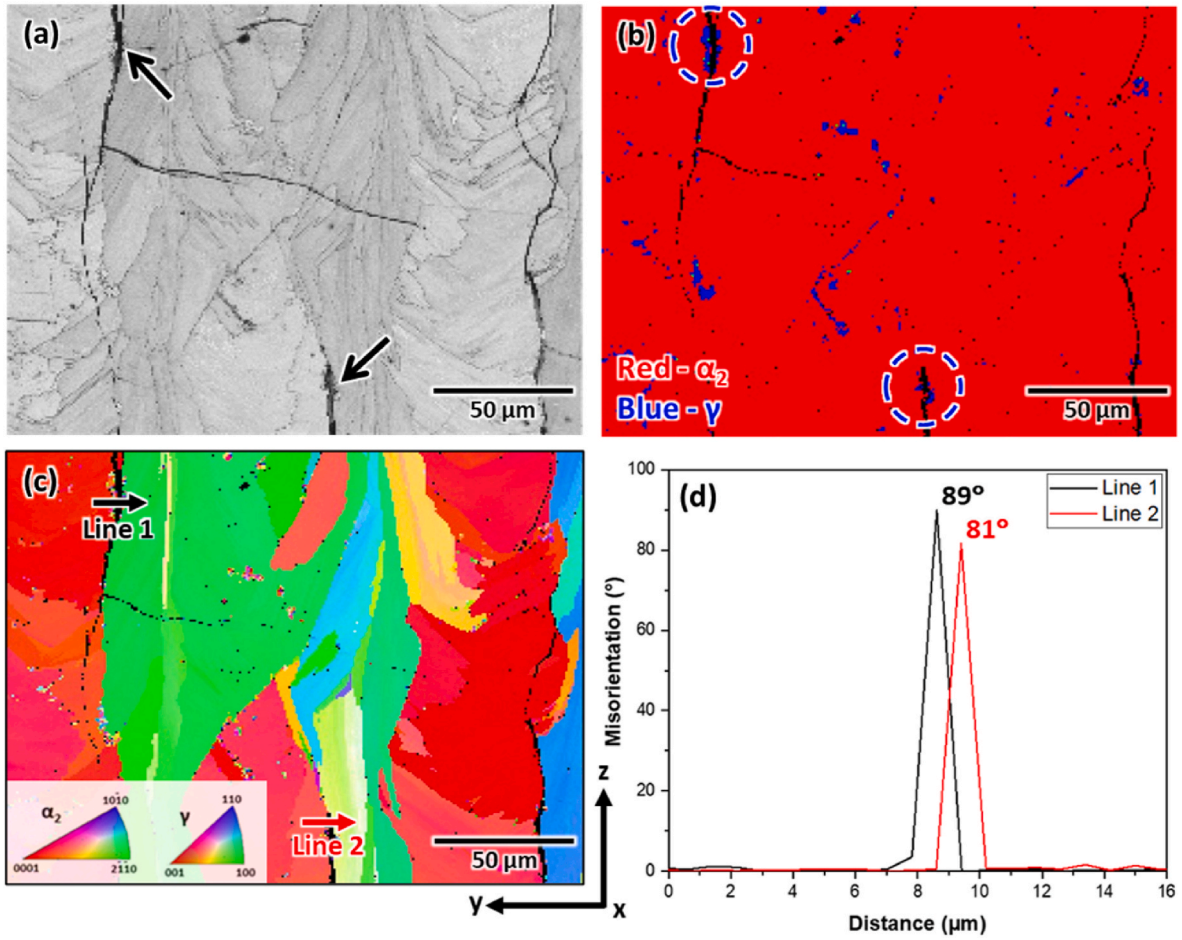

Fig. 4. (a–c) Band contrast image, phase map, and IPF map obtained from the cracking region. (d) Misorientation angle profiles between adjacent grains along lines 1 and 2 are indicated in (c).

3.3. Crystallographic texture evolution and its formation mechanism under the optimized LPBF condition

Fig. 7(a, b) shows the phase and IPF maps obtained on three orthogonal planes of the as-built sample under the optimal processing condition identified in this study. Considering only the phase constitution, the phase fractions were 97.6 ± 0.3% for the α_2 phase and 2.3 ± 0.3% for the γ phase, indicating that the microstructure was predominantly composed of the α_2 phase. In addition, the IPF maps reveal that the α_2 phase is partitioned into major and minor layers with an approximate volume fraction of 7:3, which share an identical crystal structure but exhibit distinctly different crystallographic orientations.

The corresponding partial {0001},{11 $\bar{2}$ 0}, and {10$\bar{1}$ 0} PFs of the α_2 phase within the major layer are shown in Fig. 7(c). The {0001} PF exhibits a strong intensity concentration perpendicular to the BD, whereas no localized intensity concentration is observed in the {11 $\bar{2}$ 0} and {10$\bar{1}$ 0} PFs. In contrast, the minor layer displays an opposite orientation distribution. The PFs indicate that the {0001} direction is parallel to the BD, although a slight deviation is observed, while no strongly concentrated intensity appears in the {11$\bar{2}$ 0} and {10$\bar{1}$ 0} PFs (Fig. 7(d)). Hence, the overall crystallographic texture is represented by the combined PFs shown in Fig. 7(e). It is worth noting that the CLM consisting of the major and minor layers evolves, which is commonly observed in cubic-based materials fabricated by the LPBF [45,50–52]. Although rarely addressed for crystallographic texture formation in hexagonal materials, the evolution of crystallographic texture demonstrated strong {0001} alignments along the BD, which is the so-called basal fiber texture under various process parameter conditions such as scanning strategies and scanning speed [41,53]. To the best of the authors' knowledge, the formation of the CLM in hexagonal-based materials fabricated by LPBF has not been reported.

To understand the unique CLM development in the present study, the melt pool morphology and the corresponding crystallographic texture were characterized on the y–z using the SEM image and IPF map within the same region (Fig. 8(a and b)). Black dashed lines indicate melt pool boundaries, and the red dashed line denotes the melt pool centerlines. The results reveal that the off-center region of the melt pool is associated with the formation of the major layer crystallographic texture, whereas the center of the melt pool corresponds to the minor layer. Each layer exhibits the identical crystallographic orientations that extend continuously across multiple melt pools, indicating that grains grow epitaxially along the BD.

In addition, the detailed growth directions of the elongated cellular microstructure (yellow arrows) were examined in the major and minor layers, respectively (Fig. 8(c and d)). In the off-center region of the melt pool, corresponding to the major layer, the thermal gradient is directed inward, perpendicular to the curved melt pool boundaries, and upward toward the melt pool surface. Thus, the cellular microstructure grows at approximately ±45° relative to BD. Additional observations on the x–z plane in the major layer revealed that the cellular microstructure is elongated almost parallel to the BD (Fig. 8(e−g)), which further supports that the parabolic shape of the off-center region of the melt pool generates a thermal gradient tilted by approximately ±45° relative to the BD on the y–z plane. In contrast, the curvature at the center of the melt pool is reduced and the thermal gradient becomes predominantly vertical, resulting in cellular microstructure growth along the BD. This

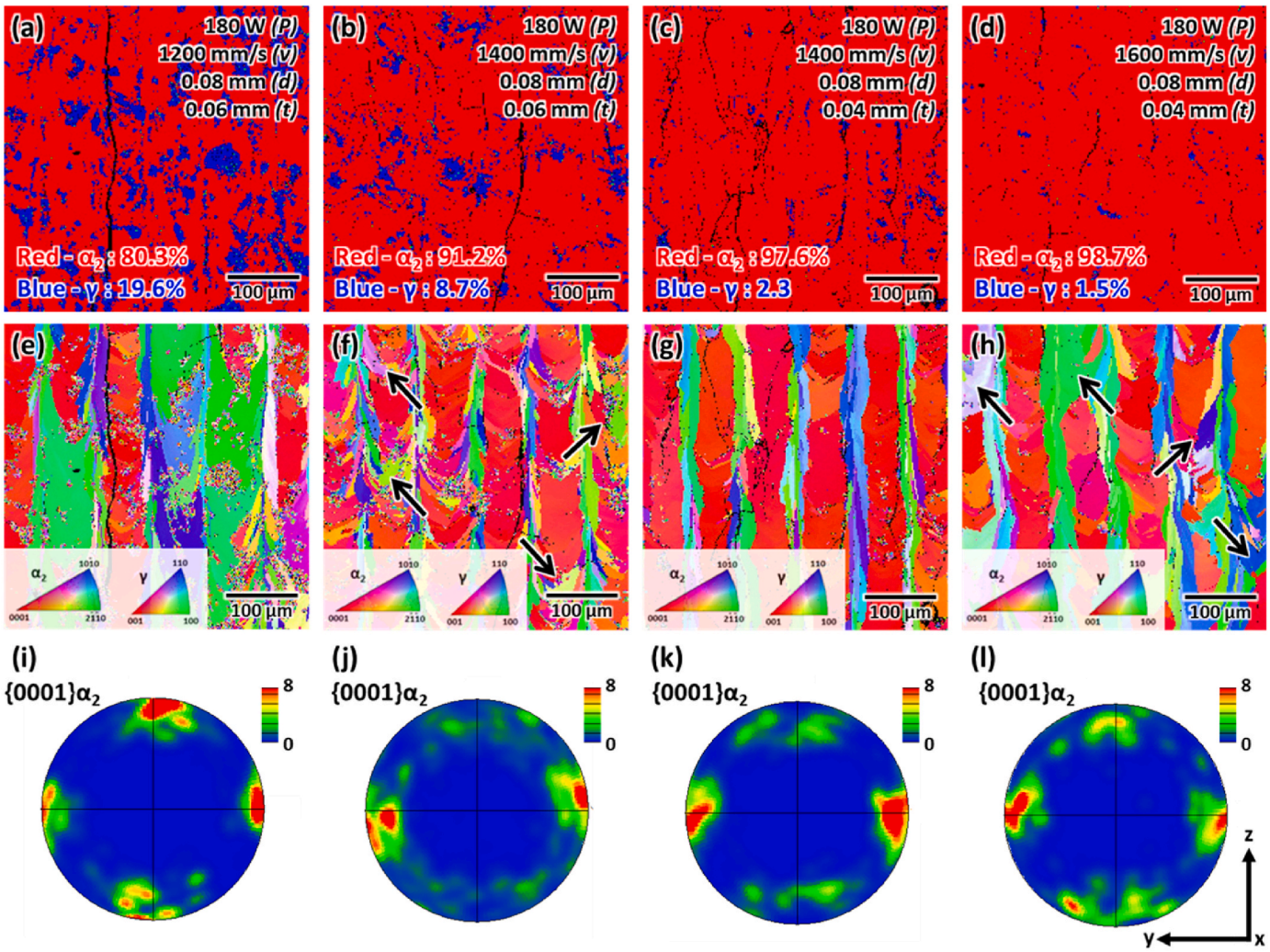

Fig. 5. (a–d) Phase maps, (e–h) IPF maps, and (i–l) {0001} PFs for the y–z plane under various process parameter conditions. Each vertical set of images corresponds to the same processing condition, and the black arrows represent the unstable epitaxial growth regions.

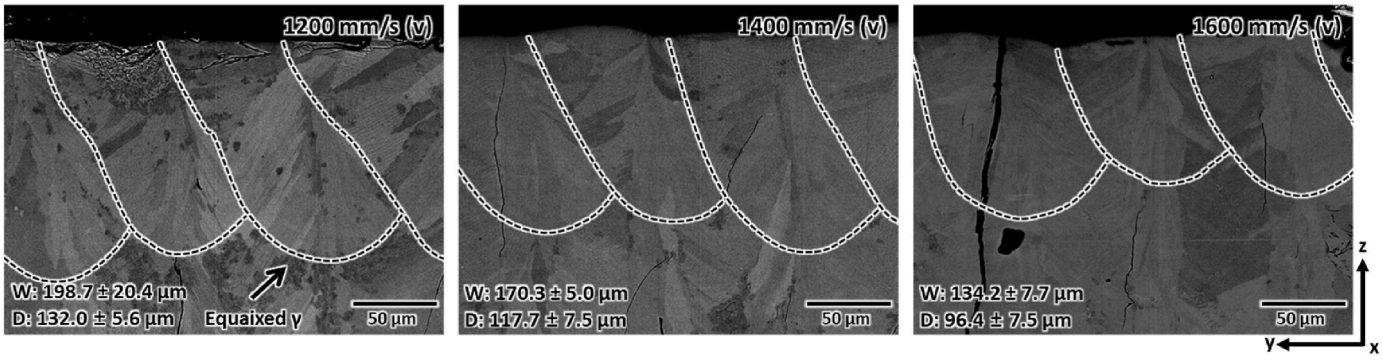

Fig. 6. Cross-sectional images taken in the y–z plane near the top surface showing melt pool morphologies at scanning speeds of (a) 1200 mm/s, (b) 1400 mm/s, and (c) 1600 mm/s.

difference in cellular growth behavior within melt pool can be explained by previously reported experimental observations and thermal simulations [45,50–52]. Under certain conditions, the thermal gradient at the bottom of the melt pool becomes well aligned with the BD, indicating that the normal direction of the solid–liquid interface is nearly parallel to the heat-flow direction. Consequently, cellular growth tends to occur along the BD in this region, which corresponds to the center of the melt pool, resulting in cellular microstructures that are elongated parallel to the BD. In contrast, in the off-center region of the melt pool, the inclined thermal gradient promotes cellular growth tilted relative to the BD, leading to the formation of differently oriented grains within the melt pool.

Considering the alloy design and microstructural observation results shown above, the unique CLM formation in this study can be depicted as

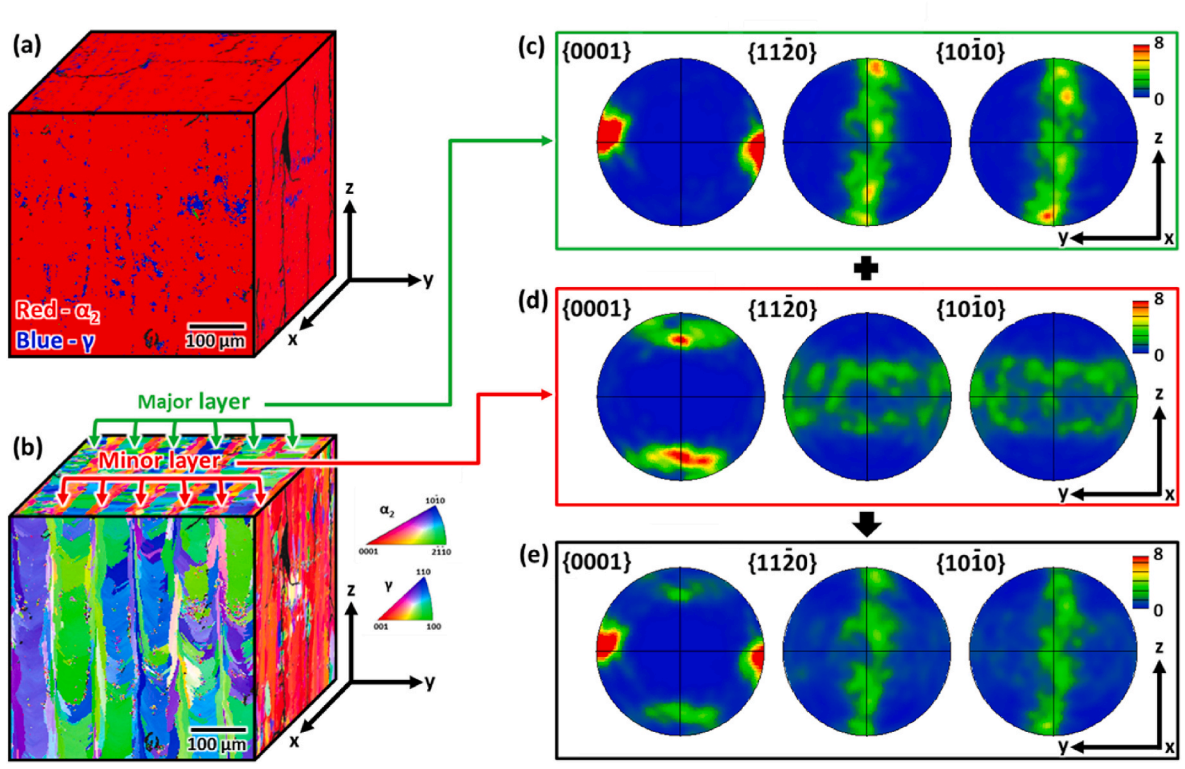

Fig. 7. (a, b) Three-dimensional images of phase and IPF maps constructed from data obtained on three orthogonal planes of the as-built sample. (c, d) Partial α_2 phase PFs from the major and minor layers, respectively. (e) Corresponding α_2 phase PFs from the overall region.

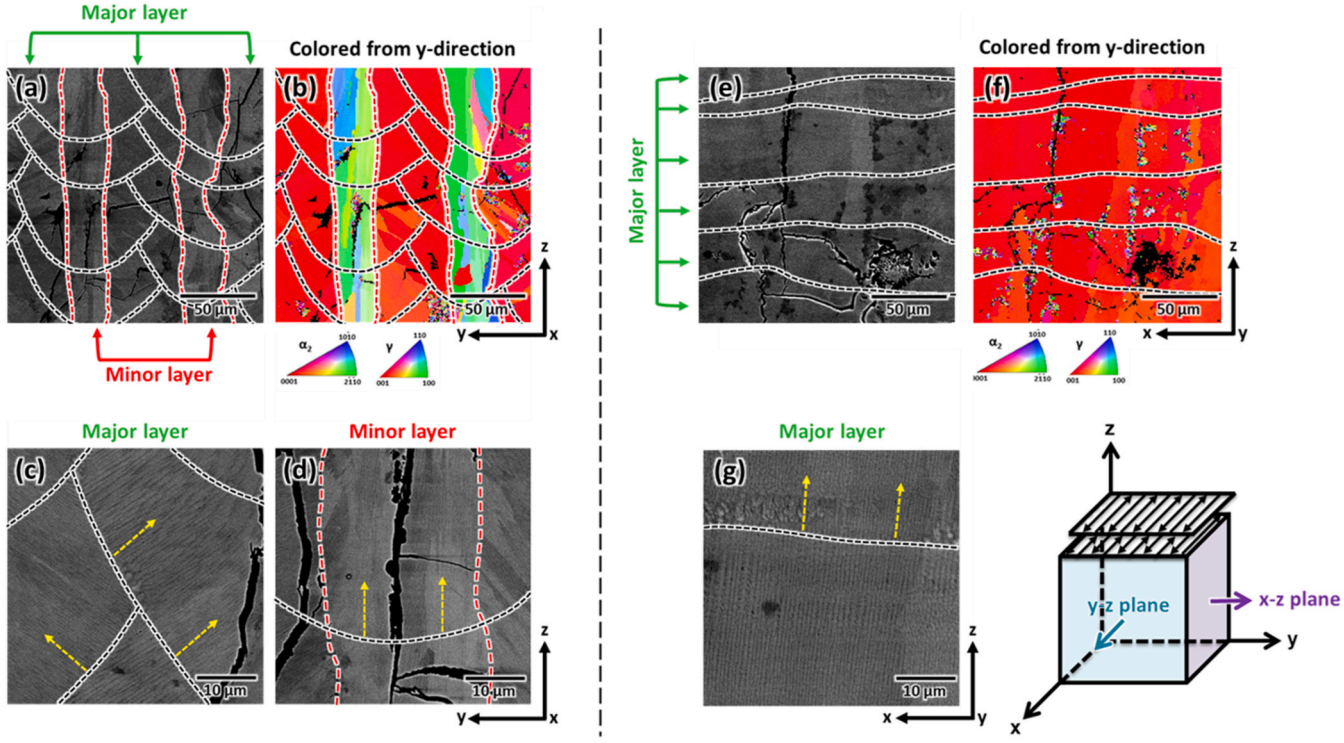

Fig. 8. (a) SEM–BSE image and (b) the corresponding IPF map from the same region on the y–z plane. (c, d) High-magnification images showing the growth direction of the cellular microstructure in the major and minor layers, respectively. (e–g) SEM–BSE image, corresponding IPF map, and high-magnification image obtained from the major layer region on the x–z plane.

illustrated in Fig. 9. The melt pool shape plays a key role in crystallographic texture formation because it is involved in the thermal gradient direction, which is generally directed perpendicular to the melt pool boundaries. Simultaneously, the elongated cell microstructures coincide

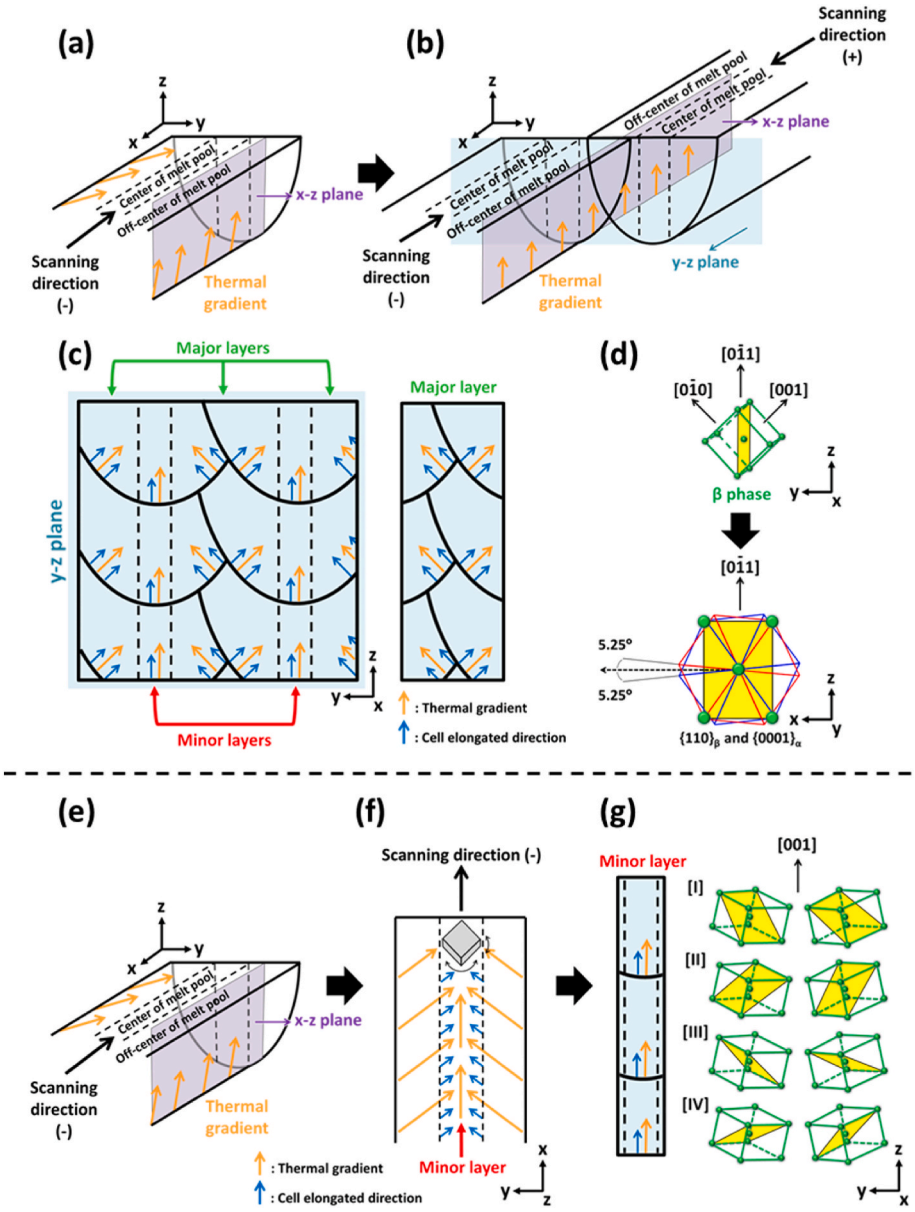

Fig. 9. Schematic illustrations of the mechanisms governing crystallographic texture evolution in the (a–d) major and (e–g) minor layers, respectively.

with the direction of the thermal gradient. For metallic materials with relatively low thermal conductivity, such as Ti-based alloys, the melt pool typically exhibits an elongated tail inclined along the laser scanning direction [54]. As a result, the thermal gradient is tilted from the vertical upward direction toward the scanning direction (Fig. 9(a)). It means that the crystal growth direction is tilted away from the BD.

However, with reciprocating laser scanning (e.g., along the +x and −x directions), the melt pools generated by successive scan tracks exhibit oppositely tilted thermal gradient directions on the x–z plane (Fig. 9(b)). When these adjacent melt pool tracks overlap, the opposing tilts effectively compensate each other, leading to a thermal gradient that is aligned in the vertical direction. Therefore, the crystal growth direction becomes self-adjusted between neighboring tracks toward a common vertical upward orientation. Such self-adjustment is likely driven by a reduction in interfacial energy associated with crystallographic misorientation at the interfaces between adjacent melt pool tracks [15,50], which are also demonstrated in the Fig. 8((e–g).

As a result, identical crystallographic orientations are established across adjacent melt pool tracks within the major layer. In addition, the parabolic shape of the melt pool y–z plane provides a thermal gradient tilted by approximately ±45° relative to the BD within the melt pool boundaries (Fig. 9(c)). Herein, because the KIMS #16 alloy was intentionally designed to undergo peritectic solidification, the α phase formed through the peritectic reaction is crystallographically inherited from the primary β phase via the Burgers OR [43,55]. Accordingly, the ±45° tilted growth behavior of the cellular microstructure can be interpreted as reflecting the primary β growth direction along <001>, which ultimately manifests as a ⟨011⟩ preferential orientation along the BD in the β phase (Fig. 9(d)). In this case, one of the six equivalent {011} planes of the β phase, highlighted in yellow, is favorably aligned with the common vertical upward thermal gradient. This alignment suggests that the corresponding {011} plane is dominantly selected during the subsequent β → α phase transformation. Therefore, the {0001} orientation of the α_2 phase is tends to align perpendicular to the BD in the major layer. However, the presence of an inherent atomic misfit (5.25°) between the β and α phases [56], induces rotations along the x and z directions, resulting in weak and dispersed orientation distribution in the {11 $\bar{2}$ 0} and {10$\bar{1}$ 0} planes.

On the other hand, in the case of the minor layer at the center of the melt pool, the microstructural evolution is influenced primarily by one-way laser scanning (Fig. 9(e)). As mentioned above, the thermal gradient is tilted from the vertical upward direction toward the scanning direction, which means that the primary β phase grows along the <001> direction inclined away from the BD (Fig. 9(f)). This tendency may become more pronounced in the present study because a relatively high v of 1400 mm/s was employed, which promote the instability of <001> crystal growth parallel to the BD at the melt pool center. In comparison, under a lower v of 1200 mm/s, the {0001} orientation of the α_2 phase was observed to form more stably parallel to the BD (Fig. 5(i)). Accordingly, although the cellular microstructure direction is observed to be parallel to the BD on the y–z plane, it is expected to be tilted in three dimensions (Figs. 8(d) and 9(g)). Such growth instability can lead to the formation of the α_2 {0001} planes from multiple possible {110} planes of the β phase, as schematically indicated by variants [I]–[IV], resulting in the {0001} of α_2 planes that are macroscopically parallel to the BD with a certain degree of deviation from the ideal orientation.

3.4. Evolution of the bi-lamellar microstructure after heat treatment

The as-built specimen fabricated under the optimized condition was heat treated at 800 °C for 3 h followed by air cooling to investigate the microstructural evolution. This heat-treatment condition was intentionally selected to examine the stability of the CLM near the typical service temperature of γ-TiAl alloys. To evaluate the phase constitution associated with this heat treatment, the typical XRD profiles of the samples before and after heat treatment were compared (Fig. 10(a)). The as-built sample consists predominantly of the α_2 phase with a minor fraction of the γ phase. After heat treatment, the predominant α_2 phase transforms into the γ phase, which is further confirmed by the phase map shown in Fig. 10(b). Interestingly, the CLM formed in the as-built specimen is maintained after heat treatment. Accordingly, the IPF map after heat treatment still exhibits the characteristic lamellar structure, consisting of the pink (major layer) and yellow (minor layer) regions (Fig. 10(c)). However, previous studies have reported that CLM structures may become unstable at higher heat-treatment temperatures (e.g., 900 °C) and can disappear due to recrystallization, leading to the formation of an equiaxed γ phase with a random crystallographic texture [57,58].

On the other hand, the γ phase generally precipitates from the α_2 phase, leading to the formation of an α_2/γ lamellar microstructure [59]. This lamellar microstructure obeys a specific orientation relationship $\{0001\}_{\alpha 2}//\{111\}_{\gamma}$ and $<11\ \bar{2}\ 0>_{\alpha 2}//<1\ \bar{1}\ 0>_{\gamma}$, which is the so-called Blackburn OR [36]. Therefore, similar intensity concentrations are observed in the PFs of both the γ and α_2 phases (Figs. 10(d and e) and Fig. 7(c and d)). Especially, the highest intensity concentration (black circled) of the $\{111\}_{\gamma}$ appears perpendicular to the BD in the major layer (Fig. 10(d)), whereas it is oriented nearly parallel to the BD in the minor layer (Fig. 10(e)). In other words, the α_2/γ lamellar direction is parallel to the BD in the major layer (0°) and nearly perpendicular to the BD in the minor layer (90°), demonstrating the establishment of a bi-directional α_2/γ lamellar microstructure.

For a more detailed observation of α_2/γ lamellar microstructure, additional TEM observations were conducted. Fig. 11(a and b) presents the example of the direct observation of α_2/γ lamellar microstructure of the main layer in the y–z plane with the corresponding selected area electron diffraction (SAED) pattern. In particular, the bright field (BF) image indicates that the α_2/γ lamellae are aligned parallel to the BD, which is more clearly observed in the inset image showing the lamellar alignment. On the other hand, Fig. 11(c and d) exhibits another set of α_2/γ lamellar microstructure, in which the BF images reveal ultrafine α_2/γ lamellae with a mean spacing of less than 15 nm. This spacing value is significantly smaller than those typically reported for conventionally processed γ-TiAl alloys, where lamellar spacings are commonly in the range of 25–50 nm depending on the alloy composition and heat

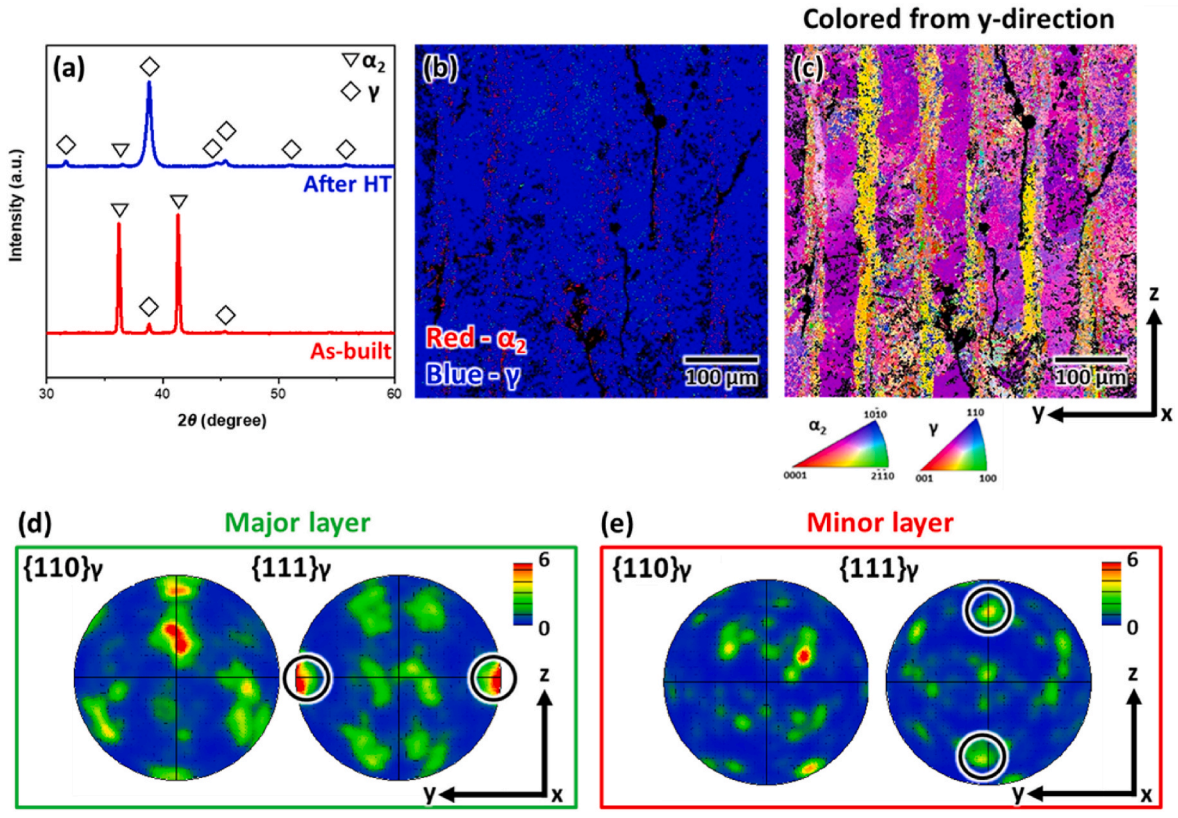

Fig. 10. (a) XRD profiles of the as-built and heat treatment samples. (b, c) Phase and IPF maps obtained on the y–z plane after heat treatment. Partial γ phase PFs corresponding to the (d) major and (e) minor layers, respectively.

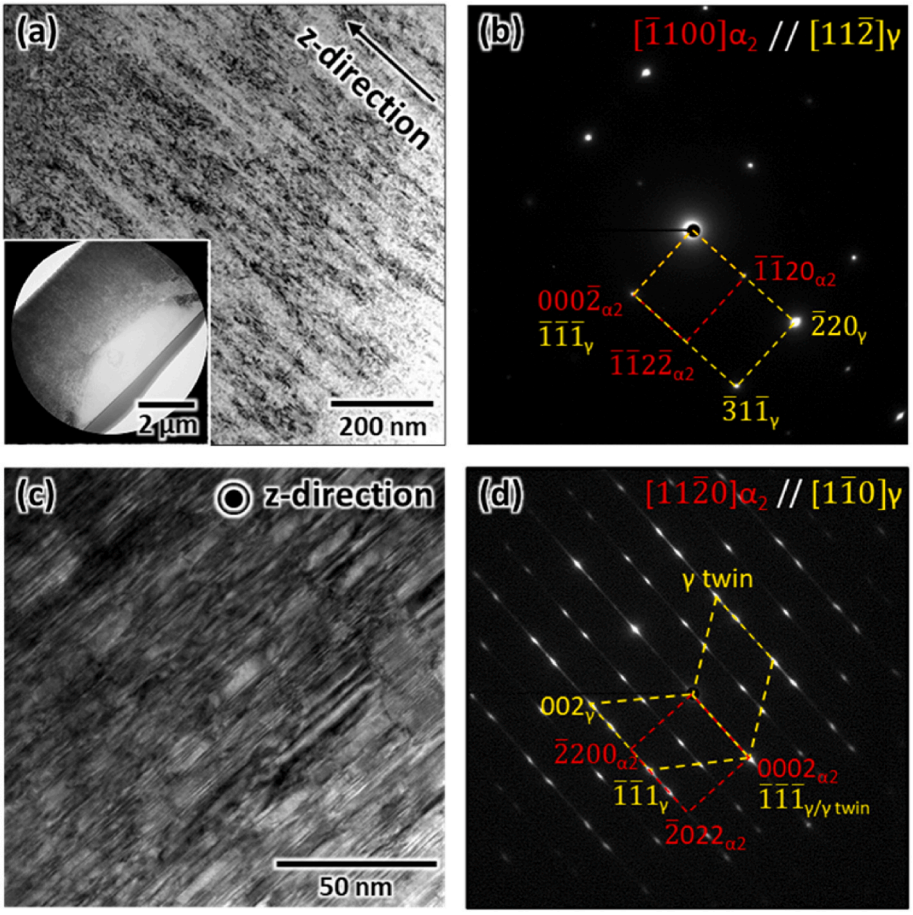

Fig. 11. (a, b) TEM image of the α_2/γ lamellar microstructure and its corresponding SAED pattern obtained from the major layer, showing α_2/γ lamellae aligned parallel to the BD. (c, d) Representative TEM image and corresponding SAED pattern, confirming the Blackburn OR of α_2/γ lamellae and γ twin.

treatment conditions [28,29]. Additionally, the corresponding SAED pattern confirms the Blackburn OR of α_2/γ lamellae and the γ twin. These results confirm that the orientation of the α_2/γ lamellar microstructure can be controlled through crystallographic texture control via the LPBF process, and followed by appropriate heat treatment.

The control of the α_2/γ lamellar orientation is strongly demanded for expanding applications of γ-TiAl alloys, as it directly governs their anisotropic mechanical properties and deformation behavior. Accordingly, the nano-indentation tests were performed to evaluate the mechanical anisotropy and the high strength associated with the controlled lamellar orientation. The measured nano-hardness was 9.3 ± 0.4 GPa for the major layer and 10.4 ± 0.8 GPa for the minor layer with the different penetration depth (Fig. 12(a and b)). Notably, both values are much higher than those of the α_2/γ lamellar microstructures of γ-TiAl alloys produced by different manufacturing processes, as summarized in Table 2.

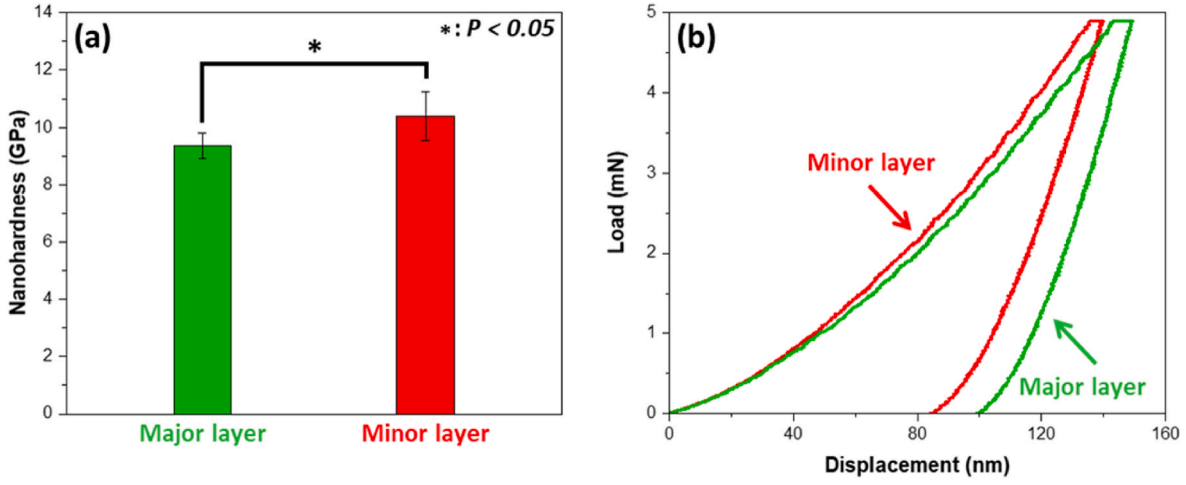

Fig. 12. (a) Average nano-hardness values of the major and minor layers along the BD, and (b) representative of the indentation load-displacement curve. *: $P < 0.05$.

Table 2
Comparison of compositions, microstructures, and corresponding nano-indentation hardness of γ-TiAl alloys fabricated by various methods.

Composition(at.%)	Fabrication	Nanohardness		
		B2 phase	α_2/γ lamellae	γ phase
Ti-44Al-6Nb-1.2Cr [60]	Arc melting		7.65 ± 0.17	
Ti-43Al-5Nb-3.5Cr-1Zr [61]	Induction skull melting	8.16 ± 0.58	7.06 ± 0.29 −8.15 ± 0.05	6.03 ± 0.66
Ti-43Al-5Nb-3.5Cr-1Zr [62]	DS	7.52 ± 0.66 −9.75 ± 0.99	6.30 ± 0.25 −7.70 ± 0.30	5.49 ± 0.49 −6.56 ± 0.31
Ti-43Al-4Nb-2Mo-0.5B [63]	Forging	8.5	6.8	5.3
Ti-43Al [64]	EB-DED		7.8 – 8.3	
Ti-46Al-6Nb-0.5W-0.5Cr-0.3Si-0.1C (This study)	LPBF		9.3 ± 0.4 −10.4 ± 0.8	

The enhancement in nano-hardness can be explained by the following factors. As represented in Fig. 11(c and d), the α_2/γ lamellar spacing of the LPBF sample after subsequent heat treatment was extremely fine. It was revealed that the ultrafast cooling rate characteristic of LPBF (on the order of 10^5 K/s) results in the formation of a supersaturated α_2 phase [27,65], and subsequent heat treatment gives rise to ultrafine lamellar spacing [39,66]. As is known, in the lamellar microstructure with densely alternating γ and α_2 plates, dislocation motion across the lamellar interfaces requires a high applied stress, thereby establishing a Hall–Petch relationship between lamellar spacing and mechanical strength [67,68]. In addition, the enhancement in nano-hardness is also attributed to the anisotropic deformation behavior of the α_2/γ lamellar microstructure. Depending on the lamellar orientation relative to the loading axis, the deformation modes can be classified into soft (45°) and hard (0° and 90°) directions, where soft directions correspond to longitudinal deformation modes with slip planes and slip directions parallel to the lamellar boundaries, whereas hard directions are governed by mixed or transverse deformation modes with slip planes inclined relative to the lamellar boundaries and slip directions either parallel or inclined [66,69]. When stress is applied to the soft direction, deformation occurs primarily in the γ phase on the {111} planes parallel to the lamellar boundaries, and slip does not pass through the lamellar interfaces. In contrast, in the hard orientation, slip on the {111} planes in the γ phase occurs across the lamellar boundaries, which increases the resistance to dislocation motion and leads to higher strength [70]. Therefore, the improved nano-hardness values originate from the ultrafine lamellar spacing and the controlled α_2/γ lamellar orientation achieved by the LPBF process.

Nevertheless, the present study does not directly demonstrate the macroscopic mechanical properties of the bi-directional α_2/γ lamellar microstructure due to the limitations of the current specimens. However, previous studies have reported that similar lamellar microstructures can lead to significant improvements in material toughness [71]. Such improvements are commonly attributed to crack-tip deflection and step-like crack propagation, and this mechanism is similar to the multiple-cracking behavior observed in laminated composite materials [72]. Therefore, although the comprehensive evaluation of macroscopic mechanical properties remains an important topic for future investigation, the present results suggest that the control of bi-directional α_2/γ lamellar microstructure may provide a new methodology for enhancing the mechanical performance of γ-TiAl alloys.

4. Conclusion

In this study, a peritectic solidification-based alloy design combined with optimized LPBF process parameters was employed to achieve crystallographic texture formation and control of the α_2/γ lamellar orientation. The main findings of this work can be summarized as follows:

1. The CLM was successfully obtained in a γ-TiAl alloy via the LPBF process, representing the first observation of such a microstructure in hexagonal materials. The CLM consists of two differently oriented crystallographically textured layers, where the {0001} direction is oriented perpendicular to the BD in the major layer and nearly parallel to the BD in the minor layer.
2. After heat treatment, the as-built CLM was preserved up to the typical service temperature range of γ-TiAl alloys and governed the orientation of the α_2/γ lamellae by Blackburn OR, leading to the formation of a bi-directional α_2/γ lamellar microstructure with lamellar orientations of 0° and 90° in the major and minor layers, respectively.
3. The controlled α_2/γ lamellar microstructure resulted in significantly enhanced nano-hardness compared with γ-TiAl alloys fabricated by other manufacturing methodologies, which is attributed to the ultrafine lamellar spacing and pronounced anisotropic mechanical behavior.

CRediT authorship contribution statement

Sung-Hyun Park: Conceptualization, Investigation, Data curation, Formal analysis, Writing – original draft. **Ozkan Gokcekaya:** Investigation, Data curation, Writing – review & editing. **Kazuhisa Sato:** Investigation, Data curation, Formal analysis. **Ji-Sung Park:** Data curation, Formal analysis. **Chae-Won Kim:** Formal analysis. **Myung-Hoon Oh:** Conceptualization, Supervision, Writing – review & editing. **Seong-Woong Kim:** Conceptualization, Resources, Supervision, Funding acquisition, Writing – review & editing. **Takayoshi Nakano:** Conceptualization, Resources, Supervision, Funding acquisition, Writing – review & editing.

Declaration of competing interest

The authors declare that they have no known competing financial interests or personal relationships that could have appeared to influence the work reported in this paper.

Acknowledgements

This work was supported by the Korean Ministry of Science and ICT (Grant Number: RS-2021-NR059196, PNKB310), Ministry of Trade, Industry and Energy (MOTIE, Grant Number:00431834), CREST-Nanomechanics: Elucidation of macroscale mechanical properties based on understanding nanoscale dynamics for innovative mechanical materials (Grant Number: JPMJCR2194) from the Japan Science and Technology Agency.

Data availability

Data will be made available on request.

References

[1] Clemens H, Mayer S. Design, processing, microstructure, properties, and applications of advanced intermetallic TiAl alloys. Adv Eng Mater 2013;15:191–215. https://doi.org/10.1002/adem.201200231.
[2] Kim Y-W, Kim S-L. Advances in gammalloy materials–processes–application technology: successes, dilemmas, and future. JOM 2018;70:553–60. https://doi.org/10.1007/s11837-018-2747-x.

[3] Bewlay BP, Nag S, Suzuki A, Weimer MJ. TiAl alloys in commercial aircraft engines. Mater High Temp 2016;33:549–59. https://doi.org/10.1080/09603409.2016.1183068.

[4] Chen G, Peng Y, Zheng G, Qi Z, Wang M, Yu H, et al. Polysynthetic twinned TiAl single crystals for high-temperature applications. Nat Mater 2016;15:876–81. https://doi.org/10.1038/nmat4677.

[5] Johnson DR, Inui H, Yamaguchi M. Directional solidification and microstructural control of the TiAl/Ti_3Al lamellar microstructure in TiAl-Si alloys. Acta Mater 1996;44:2523–35. https://doi.org/10.1016/1359-6454(95)00338-X.

[6] Yamaguchi M, Johnson DR, Lee HN, Inui H. Directional solidification of TiAl-base alloys. Intermetallics 2000;8:511–7. https://doi.org/10.1016/S0966-9795(99)00157-0.

[7] Lee HN, Johnson DR, Inui H, Oh MH, Wee DM, Yamaguchi M. Microstructural control through seeding and directional solidification of TiAl alloys containing Mo and C. Acta Mater 2000;48:3221–33. https://doi.org/10.1016/S1359-6454(00)00123-3.

[8] Kim JH, Kim SW, Lee HN, Oh MH, Inui H, Wee DM. Effects of Si and C additions on the thermal stability of directionally solidified TiAl-Nb alloys. Intermetallics 2005;13:1038–47. https://doi.org/10.1016/j.intermet.2004.10.010.

[9] Frazier WE. Metal additive manufacturing: a review. J Mater Eng Perform 2014;23:1917–28. https://doi.org/10.1007/s11665-014-0958-z.

[10] Li Y, Wu H, Ding F, Hao R, Lei M, Li X, et al. Exceptional strength–ductility–modulus combination in additively manufactured metastable β titanium alloy via synergistic tuning of strengthening mechanisms. Mater Sci Eng, A 2026;959. https://doi.org/10.1016/j.msea.2026.150057.

[11] Fan A, Luo H, Liao J, Du Y. Influence of zinc evaporation-driven spattering on defect formation and mechanical properties in laser powder bed fusion of AA7075 aluminum alloy. J Mater Res Technol 2026;41:2335–48. https://doi.org/10.1016/j.jmrt.2026.01.174.

[12] Bao Z, Lian L, Wu J, Liu Y. Process-parameter-dependent defects formation mechanisms in laser powder bed fusion of non-weldable nickel-based superalloy. J Mater Res Technol 2026;41:2534–55. https://doi.org/10.1016/j.jmrt.2026.01.177.

[13] Yao G-R, Chang C, Cox SC, Zhang X-F, Yang C, Li X-Q, et al. Establishing the intrinsic connection between microstructure, 3D defects, and the corrosion behavior of selective laser melted WE43 alloys. Rare Met 2025;44:9217–34. https://doi.org/10.1007/s12598-025-03463-z.

[14] Luo X, Song T, Gebert A, Neufeld K, Kaban I, Ma H, et al. Programming crystallographic orientation in additive-manufactured beta-type titanium alloy. Adv Sci 2023;10. https://doi.org/10.1002/advs.202302884.

[15] Ishimoto T, Morita N, Ozasa R, Matsugaki A, Gokcekaya O, Higashino S, et al. Superimpositional design of crystallographic textures and macroscopic shapes via metal additive manufacturing—Game-change in component design. Acta Mater 2025;286. https://doi.org/10.1016/j.actamat.2025.120709.

[16] Park SH, Ayten F, Bulutsuz AG, Gokcekaya O, İlgazi ME, Yilmazer H, et al. Wear and corrosion performance of textured Hastelloy-X fabricated by laser powder bed fusion: process window and microstructural features. J Mater Res Technol 2025;39:6156–68. https://doi.org/10.1016/j.jmrt.2025.10.229.

[17] Park SH, Gokcekaya O, Nitomakida T, Nakano T. Effects of heat accumulation strategies on defects and microstructure of pure chromium fabricated by laser powder bed fusion: an experimental and numerical study. J Mater Res Technol 2024. https://doi.org/10.1016/j.jmrt.2024.11.049.

[18] Gokcekaya O, Ishimoto T, Nishikawa Y, Kim YS, Matsugaki A, Ozasa R, et al. Novel single crystalline-like non-equiatomic TiZrHfNbTaMo bio-high entropy alloy (BioHEA) developed by laser powder bed fusion. Mater Res Lett 2023;11:274–80. https://doi.org/10.1080/21663831.2022.2147406.

[19] Gokcekaya O, Ishimoto T, Todo T, Wang P, Nakano T. Influence of powder characteristics on densification via crystallographic texture formation: pure tungsten prepared by laser powder bed fusion. Addit Manuf Lett 2021;1:100016. https://doi.org/10.1016/j.addlet.2021.100016.

[20] Nazari-Onlaghi S, Li G, Vanmeensel K, Seefeldt M. Deformation texture in LPBF 316L studied by different crystal plasticity models. Mater Sci Eng, A 2025;924. https://doi.org/10.1016/j.msea.2024.147769.

[21] Shi G, Li L, Yu Z, Sha P, Cao Q, Xu Z, et al. Effect of crystallographic anisotropy on phase transformation and tribological properties of Ni-rich NiTi shape memory alloy fabricated by LPBF. Opt Laser Technol 2023;157. https://doi.org/10.1016/j.optlastec.2022.108731.

[22] Wang MS, Liu EW, Du YL, Liu TT, Liao WH. Cracking mechanism and a novel strategy to eliminate cracks in TiAl alloy additively manufactured by selective laser melting. Scr Mater 2021;204:114151. https://doi.org/10.1016/j.scriptamat.2021.114151.

[23] Park SH, Gokcekaya O, Oh MH, Nakano T. Effects of hatch spacing on densification, microstructural and mechanical properties of β-solidifying γ-TiAl alloy fabricated by laser powder bed fusion. Mater Char 2024;214. https://doi.org/10.1016/j.matchar.2024.114077.

[24] Lee S, Kim J, Choe J, Kim SW, Hong JK, Choi YS. Understanding crack formation mechanisms of Ti–48Al–2Cr–2Nb single tracks during laser powder bed fusion. Met Mater Int 2020. https://doi.org/10.1007/s12540-020-00770-1.

[25] Gao P, Huang W, Yang H, Jing G, Liu Q, Wang G, et al. Cracking behavior and control of β-solidifying Ti-40Al-9V-0.5Y alloy produced by selective laser melting. J Mater Sci Technol 2020;39:144–54. https://doi.org/10.1016/j.jmst.2019.08.026.

[26] Gao P, Lan X, Yang S, Wang Z, Li X, Cao L. Defect elimination and microstructure improvement of laser powder bed fusion β-solidifying γ-TiAl alloys via circular beam oscillation technology. Mater Sci Eng, A 2023;873. https://doi.org/10.1016/j.msea.2023.145019.

[27] Wang M, Du Y, Wei H, Liao W. From crack-prone to crack-free: eliminating cracks in additively manufactured Ti-48Al-2Cr-2Nb alloy by adjusting phase composition. Mater Des 2023;231. https://doi.org/10.1016/j.matdes.2023.112025.

[28] Schwaighofer E, Clemens H, Mayer S, Lindemann J, Klose J, Smarsly W, et al. Microstructural design and mechanical properties of a cast and heat-treated intermetallic multi-phase γ-TiAl based alloy. Intermetallics 2014;44:128–40. https://doi.org/10.1016/j.intermet.2013.09.010.

[29] Zheng G, Tang B, Zhao S, Wang WY, Chen X, Zhu L, et al. Evading the strength-ductility trade-off at room temperature and achieving ultrahigh plasticity at 800°C in a TiAl alloy. Acta Mater 2022;225. https://doi.org/10.1016/j.actamat.2021.117585.

[30] Gao Z, Hu R, Zou H, Li J, Zhou M, Luo X. Metastable microstructure evolution and grain refinement in a Low-Ta containing γ-TiAl alloy through heat treatment. J Mater Res Technol 2024;29:3642–55. https://doi.org/10.1016/j.jmrt.2024.02.095.

[31] Zhang X, Li C, Zheng M, Ye Z, Yang X, Gu J. Anisotropic tensile behavior of Ti-47Al-2Cr-2Nb alloy fabricated by direct laser deposition. Addit Manuf 2020;32. https://doi.org/10.1016/j.addma.2020.101087.

[32] Zhang X, Ye Z, Li C, Gu J. Microstructures and mechanical behaviors of a directional lamellar Ti-48Al-2Cr-2Nb alloy produced by laser additive manufacturing. Mater Char 2024;218. https://doi.org/10.1016/j.matchar.2024.114470.

[33] Ding X, Zhang L, He J, Zhang F, Feng X, Nan H, et al. As-cast microstructure characteristics dependent on solidification mode in TiAl-Nb alloys. J Alloys Compd 2019;809. https://doi.org/10.1016/j.jallcom.2019.151862.

[34] Ding X, Liu H, Zhang F, Zhang L, Huang H, Nan H, et al. Microstructure characteristics of the directionally solidified TiAl-Nb alloys with different solidification modes. Mater Today Commun 2022;32. https://doi.org/10.1016/j.mtcomm.2022.103770.

[35] Burgers WG. On the process of transition of the cubic-body-centered modification into the hexagonal-close-packed modification of zirconium. Physica 1934;1:561–86. https://doi.org/10.1016/S0031-8914(34)80244-3.

[36] Blackburn MJ. Some aspects of phase transformations in titanium alloys. In: The science, technology and application of titanium. Elsevier; 1970. p. 633–43. https://doi.org/10.1016/b978-0-08-006564-9.50071-3.

[37] Wang SC, Aindow M, Starink MJ. Effect of self-accommodation on α/α boundary populations in pure titanium. Acta Mater 2003;51:2485–503. https://doi.org/10.1016/S1359-6454(03)00035-1.

[38] Bhattacharyya D, Viswanathan GB, Denkenberger R, Furrer D, Fraser HL. The role of crystallographic and geometrical relationships between α and β phases in an α/β titanium alloy. Acta Mater 2003;51:4679–91. https://doi.org/10.1016/S1359-6454(03)00179-4.

[39] Cho K, Kawabata H, Hayashi T, Yasuda HY, Nakashima H, Takeyama M, et al. Peculiar microstructural evolution and tensile properties of β-containing γ-TiAl alloys fabricated by electron beam melting. Addit Manuf 2021;46:102091. https://doi.org/10.1016/j.addma.2021.102091.

[40] Kim SE, Lee YT, Oh MH, Inui H, Yamaguchi M. Directional solidification of TiAl-Si alloys using polycrystalline seed. Intermetallics 2000;8:399–405. https://doi.org/10.1016/S0966-9795(99)00122-3.

[41] Hagihara K, Ishimoto T, Suzuki M, Ozasa R, Matsugaki A, Wang P, et al. Factor which governs the feature of texture developed during additive manufacturing; clarified from the study on hexagonal C40-NbSi2. Scr Mater 2021;203. https://doi.org/10.1016/j.scriptamat.2021.114111.

[42] Ding XF, Lin JP, Zhang LQ, Su YQ, Wang HL, Chen GL. Lamellar orientation control in a Ti-46Al-5Nb alloy by directional solidification. Scr Mater 2011;65:61–4. https://doi.org/10.1016/j.scriptamat.2011.02.011.

[43] Duan B, Yang Y, He S, Feng Q, Mao L, Zhang X, et al. History and development of γ-TiAl alloys and the effect of alloying elements on their phase transformations. J Alloys Compd 2022;909. https://doi.org/10.1016/j.jallcom.2022.164811.

[44] Staron P, Stark A, Schell N, Spoerk-Erdely P, Clemens H. Thermal expansion of a multiphase intermetallic ti-al-nb-mo alloy studied by high-energy X-ray diffraction. Materials 2021;14:727. https://doi.org/10.3390/ma14040727.

[45] Gokcekaya O, Ishimoto T, Hibino S, Yasutomi J, Narushima T, Nakano T. Unique crystallographic texture formation in Inconel 718 by laser powder bed fusion and its effect on mechanical anisotropy. Acta Mater 2021;212:116876. https://doi.org/10.1016/j.actamat.2021.116876.

[46] Sun S-H, Ishimoto T, Hagihara K, Tsutsumi Y, Hanawa T, Nakano T. Excellent mechanical and corrosion properties of austenitic stainless steel with a unique crystallographic lamellar microstructure via selective laser melting. Scr Mater 2019;159:89–93. https://doi.org/10.1016/j.scriptamat.2018.09.017.

[47] Huang D, Zhou Y, Yao X, Tan Q, Chang H, Wang D, et al. From crack-prone to crack-free: unravelling the roles of LaB6 in a β-solidifying TiAl alloy fabricated with laser additive manufacturing. Mater Sci Eng, A 2022;861. https://doi.org/10.1016/j.msea.2022.144358.

[48] Martin JH, Yahata BD, Hundley JM, Mayer JA, Schaedler TA, Pollock TM. 3D printing of high-strength aluminium alloys. Nature 2017;549:365–9. https://doi.org/10.1038/nature23894.

[49] Mizuta K, Hijikata Y, Fujii T, Gokan K, Kakehi K. Characterization of Ti-48Al-2Cr-2Nb built by selective laser melting. Scr Mater 2021;203. https://doi.org/10.1016/j.scriptamat.2021.114107.

[50] Sofinowski KA, Raman S, Wang X, Gaskey B, Seita M. Layer-wise engineering of grain orientation (LEGO) in laser powder bed fusion of stainless steel 316L. Addit Manuf 2021;38:101809. https://doi.org/10.1016/j.addma.2020.101809.

[51] Cho K, Yamashita K, Kakutani S, Saito T, Sasaki T, Sawaizumi K, et al. Effect of nanoscale cellular structure on the mechanical properties of Inconel 718 with

unique hierarchical structure fabricated by laser powder bed fusion. Acta Mater 2026;303. https://doi.org/10.1016/j.actamat.2025.121696.
[52] Chen G, Wang X, Yang X, Wang J, Zhang T, Zhang Z, et al. Unexpected heterogeneous texture in laser beam powder bed fusion under fixed process parameters. Mater Des 2025;259. https://doi.org/10.1016/j.matdes.2025.114867.
[53] Esmaily M, Zeng Z, Mortazavi AN, Gullino A, Choudhary S, Derra T, et al. A detailed microstructural and corrosion analysis of magnesium alloy WE43 manufactured by selective laser melting. Addit Manuf 2020;35. https://doi.org/10.1016/j.addma.2020.101321.
[54] Todo T, Ishimoto T, Gokcekaya O, Oh J, Nakano T. Single crystalline-like crystallographic texture formation of pure tungsten through laser powder bed fusion. Scr Mater 2022;206:114252. https://doi.org/10.1016/j.scriptamat.2021.114252.
[55] Ding XF, Lin JP, Zhang LQ, Su YQ, Hao GJ, Chen GL. A closely-complete peritectic transformation during directional solidification of a Ti-45Al-8.5Nb alloy. Intermetallics 2011;19:1115–9. https://doi.org/10.1016/j.intermet.2011.03.005.
[56] Kan W, Chen B, Peng H, Liang Y, Lin J. Formation of columnar lamellar colony grain structure in a high Nb-TiAl alloy by electron beam melting. J Alloys Compd 2019;809. https://doi.org/10.1016/j.jallcom.2019.151673.
[57] Liu S, Ding H, Chen R, Guo J, Fu H. Evolution of rapidly grown cellular microstructure during heat treatment of TiAl-based intermetallic and its effect on micromechanical properties. Intermetallics 2021;132. https://doi.org/10.1016/j.intermet.2021.107166.
[58] Guyon J, Hazotte A, Wagner F, Bouzy E. Recrystallization of coherent nanolamellar structures in Ti48Al2Cr2Nb intermetallic alloy. Acta Mater 2016;103:672–80. https://doi.org/10.1016/j.actamat.2015.10.049.
[59] Denquint A, Naka S. Phase transformation mechanisms involved in two-phase TiAl-based alloys–I. Lambellar structure formation. Acta Mater 1996;44:343–52. https://doi.org/10.1016/1359-6454(95)00167-4.
[60] Park SH, Gokcekaya O, Ozasa R, Oh MH, Kim YW, Kim HS, et al. Microstructure and crystallographic texture evolution of β-Solidifying γ-TiAl alloy during Single- and multi-track exposure via laser powder bed fusion. Met Mater Int 2024;30:1227–41. https://doi.org/10.1007/s12540-023-01579-4.
[61] Song H, Xu X, Ding H, Zhang X, Chen R, Guo J, et al. Microstructure and nanomechanical behavior of individual phase in β-solidifying Ti-43Al-5Nb-3.5Cr-1Zr alloy. J Mater Res Technol 2022;18:1081–91. https://doi.org/10.1016/j.jmrt.2022.03.019.
[62] Xu X, Ding H, Huang H, Liang H, Kawk S, Chen R, et al. Role of growth rate on microstructure evolution, element distribution and nanohardness of phases in directionally solidified multiphase high-Nb TiAl alloy. J Mater Res Technol 2021;14:2884–96. https://doi.org/10.1016/j.jmrt.2021.08.104.
[63] Niu HZ, Chen YY, Xiao SL, Xu LJ. Microstructure evolution and mechanical properties of a novel beta γ-TiAl alloy. Intermetallics 2012;31:225–31. https://doi.org/10.1016/j.intermet.2012.07.012.
[64] Lv Q, Wang L, Liu C, Tan Y-M, Su B-X, Wang B-B, et al. Nano-lamellar Ti_3Al/TiAl alloy prepared via dual-wire-fed electron beam-directed energy deposition: microstructure evolution and nanohardness enhancement. Rare Metals 2025;44:1312–31. https://doi.org/10.1007/s12598.
[65] Zhang X, Mao B, Mushongera L, Kundin J, Liao Y. Laser powder bed fusion of titanium aluminides: an investigation on site-specific microstructure evolution mechanism. Mater Des 2021;201. https://doi.org/10.1016/j.matdes.2021.109501.
[66] Palomares-García AJ, Sabirov I, Pérez-Prado MT, Molina-Aldareguia JM. Effect of nanoscale thick lamellae on the micromechanical response of a TiAl alloy. Scr Mater 2017;139:17–21. https://doi.org/10.1016/j.scriptamat.2017.06.002.
[67] Cha L, Scheu C, Clemens H, Chladil HF, Dehm G, Gerling R, et al. Nanometer-scaled lamellar microstructures in Ti-45Al-7.5Nb-(0; 0.5)C alloys and their influence on hardness. Intermetallics 2008;16:868–75. https://doi.org/10.1016/j.intermet.2008.03.009.
[68] Panov DO, Sokolovsky VS, Stepanov ND, Zherebtsov SV, Panin PV, Volokitina EI, et al. Effect of interlamellar spacing on strength-ductility combination of β-solidified γ-TiAl based alloy with fully lamellar structure. Mater Sci Eng, A 2023;862. https://doi.org/10.1016/j.msea.2022.144458.
[69] Palomares-García AJ, Pérez-Prado MT, Molina-Aldareguia JM. Effect of lamellar orientation on the strength and operating deformation mechanisms of fully lamellar TiAl alloys determined by micropillar compression. Acta Mater 2017;123:102–14. https://doi.org/10.1016/j.actamat.2016.10.034.
[70] Umakoshi Y, Nakano T. The role of ordered domains and slip mode of α2 phase in the plastic behaviour of TiAl crystals containing oriented lamellae. Acta Metall Mater 1993;41:1155–61. https://doi.org/10.1016/0956-7151(93)90163-M.
[71] Hagihara K, Ikenishi T, Nakano T. Development of unique cross-lamellar microstructure, resulting in the drastic increase in fracture toughness in Cr/Ir-codoped (Mo0.85Nb0.15)Si2 crystals. Scr Mater 2017;131:19–23. https://doi.org/10.1016/j.scriptamat.2016.12.029.
[72] Hwu KL, Derby B. Fracture of metal/ceramic laminates–I. Transition from single to multiple cracking. Acta Mater 1999;47:529–43. https://doi.org/10.1016/S1359-6454(98)00357-7.